J. Fluid Mech. (2025), *vol*. 1002, A40, doi:10.1017/jfm.2024.1225

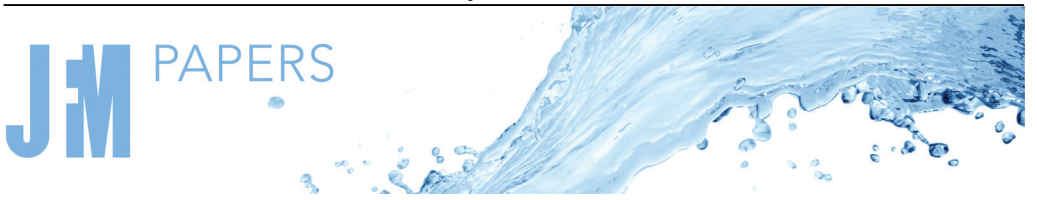

Controlled Haines jumps in a dual-channel multiphase system: inferring fluid properties from the dynamics of interface motion

Zhongzheng Wang[1,†], Runze Sun[2], Yixiang Gan[3,4], Jean-Michel Pereira[5], Scott W. McCue[6] and Emilie Sauret[1,†]

[1]School of Mechanical, Medical and Process Engineering, Queensland University of Technology, QLD 4001, Australia

[2]School of Mechanical Engineering, Hebei University of Technology, 300000 Tianjin, PR China

[3]School of Civil Engineering, The University of Sydney, NSW 2006, Australia

[4]Sydney Nano, The University of Sydney, NSW 2006, Australia

[5]Navier, Ecole des Ponts, Univ Gustave Eiffel, CNRS, 77420 Marne-la-Vallée, France

[6]School of Mathematical Sciences, Queensland University of Technology, Brisbane, QLD 4001, Australia

(Received 7 March 2024; revised 15 November 2024; accepted 17 December 2024)

When one fluid is injected into a confined geometry such as a porous medium filled with another immiscible fluid, even at an extremely low injection speed, rapid filling of several pore spaces accompanied by retraction of multiple fluid–fluid interfaces can be observed. Such processes with fast liquid redistribution within the solid structure, called Haines jumps, are ubiquitous in many multiphase flow systems, which can impact fluid trapping, energy dissipation and hysteretic saturation in various engineering applications. Inspired by this mechanism, here, we propose a dual-channel structure to realise controlled Haines jumps during fluid displacement processes. Via theoretical analysis and numerical simulations, we show that the dynamics of fluid interfaces during Haines jumps can be quantitatively correlated with the driving capillary pressure and dissipating viscous stress, which enables simultaneous determination of the fluid viscosity and interfacial tension in the dual-channel multiphase system.

Key words: Hele-Shaw flows, microfluidics, multiphase flow

† Email addresses for correspondence: zhongzheng.wang@qut.edu.au, emilie.sauret@qut.edu.au

1. Introduction

Haines jumps occur during the displacement of one fluid by another in porous materials. This process involves rapid redistribution of the liquid, quick movements of the fluid interfaces and fluctuations in pressure (Haines 1930). Haines jumps have profound implications for fluid trapping, energy dissipation and saturation hysteresis, relevant to various engineering applications including enhanced oil recovery (Lake *et al.* 2014), carbon geosequestration (Szulczewski *et al.* 2012) and underground hydrogen storage (Heinemann *et al.* 2021). As a result, the dynamics of Haines jumps has been examined in porous rocks (Berg *et al.* 2013), Hele-Shaw cells (Furuberg, Måløy & Feder 1996; Armstrong *et al.* 2015; Holtzman *et al.* 2023) and irregular capillaries (Moebius & Or 2012; Jang, Sun & Santamarina 2016). Through microfluidic experiments, Sun & Santamarina (2019) showed that the mechanisms triggering Haines jumps include the deformation of solids, compression of fluids and interactions of multiple menisci. Armstrong *et al.* (2015) investigated the influence zone of Haines jumps under different fluid properties in porous medium micro-models, and revealed the inverse relationship between a Haines jump's time and length scales.

Fundamentally, the dynamics of a Haines jump is a manifestation of the competition between viscous and capillary forces at the pore scale. As a result, apart from being a qualitative indicator of flow regimes of fluid displacement processes, we hypothesise that it can be utilised to quantitatively determine the fluid properties in the multiphase system. Thus, the objectives of this work are to answer the following questions: (i) How can we induce controlled Haines jumps in microfluidic devices, and (ii) how can this be used to infer the fluid properties? Here, we propose a dual-channel structure with a carefully selected geometry. Numerical simulations are conducted for immiscible fluid displacement under various fluid properties in the dual-channel system. Following the characterisation of the fast interface motion during Haines jumps, an analytical model is developed to describe the liquid redistribution process. We show that the fluid viscosity and interfacial tension can be simultaneously determined by analysing the interfacial dynamics during a single Haines jump.

2. Methods

2.1. *Geometry of the dual-channel system*

The key geometrical feature of our dual-channel geometry is the presence of a width contrast between the two channels and the hierarchies of capillary resistances such that the injected fluid first invades the narrower (top) channel (in the case of the drainage process, corresponding to a contact angle $\theta > 90^\circ$, which is the angle measured within the invading fluid at the triple-contact line) such that the Haines jump can be initialised when gaining access to the bottom channel that has a wider width associated with smaller capillary resistance.

Figure 1(*a*) shows the schematic of the proposed dual-channel system geometry (not to scale). The top channel has a width of $h_{top} = 0.7$ mm, being smaller than the bottom channel width of $h_{bot} = 1$ mm. The two channels are separated by a thin wall $d = 0.1$ mm in width and $W = 15$ mm in length. The inlet and outlet channels have the same dimensions of $l_{in} = l_{out} = 1$ mm in length and $h_{in} = h_{out} = 1$ mm in width. Triangular barriers are placed at the front and rear sides of the bottom and top channels, respectively, reducing the corresponding channel width at respective locations, such that the width at the entrance of the bottom channel is $h_{top} = 0.7$ mm, and the width at the rear of the top channel is $h_{neck} = 0.5$ mm.

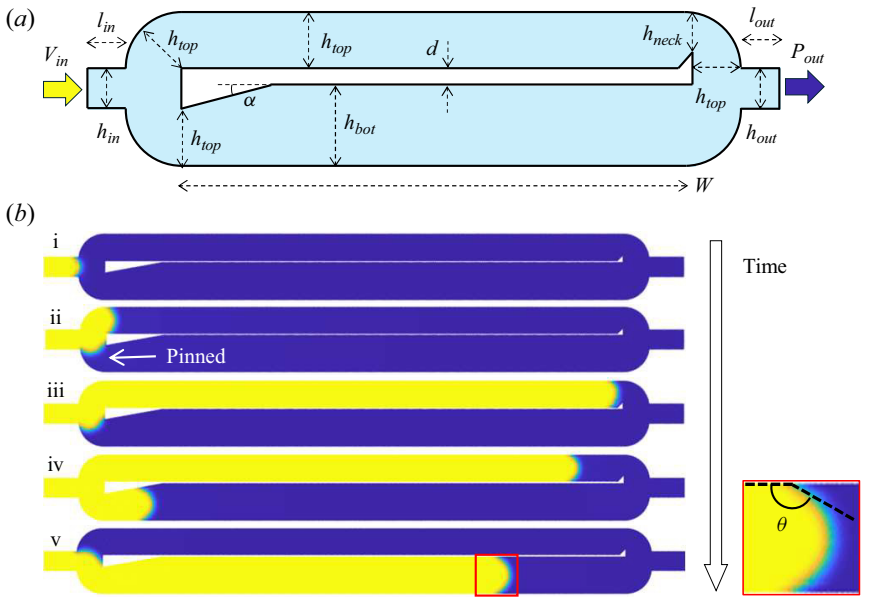

Figure 1. A Haines jump in the dual-channel multiphase system. (*a*) A schematic showing the geometry and dimensions (not to scale). The uniform channel depth D (out-of-plane direction) is not shown in the two-dimensional schematic. (*b*) Snapshots of simulated fluid invasion process in the proposed microfluidic device. The invading fluid is coloured in yellow and the defending fluid is coloured in blue. Images (iii) to (v) correspond to the Haines jump. The inset shows the contact angle θ which is measured within the invading phase.

Case number	μ_{inv} (Pa · s)	μ_{def} (Pa · s)	Viscosity ratio M	σ (N m^{-1})	θ (°)
1	0.010	0.001	1/10	0.07	141
2	0.010	0.001	1/10	0.15	141
3	0.003	0.001	1/3	0.07	141
4	0.001	0.003	3	0.07	141
5	0.001	0.010	10	0.07	141
6	0.001	0.010	10	0.15	141
7	0.002	0.002	1	0.07	141
8	0.002	0.002	1	0.04	141
9	0.002	0.002	1	0.07	134

Table 1. Fluid properties in the simulations.

We can rationalise the design of the dual-channel system by examining an example of a fluid displacement process from a numerical simulation shown in figure 1(*b*), with the dynamic viscosities for invading (yellow) and defending (blue) fluids being $\mu_{inv} = 0.001$ Pa · s and $\mu_{def} = 0.003$ Pa · s, respectively, an interfacial tension of $\sigma = 0.07$ N m^{-1}, a contact angle of $\theta = 141^\circ$ (a drainage process) and a constant inlet velocity $V_{in} = 1$ mm s^{-1}. The viscosity ratio is $M = \mu_{def}/\mu_{inv} = 3$. These fluid properties correspond to case 4 as shown in table 1.

When the invading fluid reaches the front (left side) of the middle wall (the thin wall separating the two channels), the radii of both the top and bottom arc are both $h_{top} = 0.7$ mm, implying equal capillary resistance. However, as the menisci move forward, the

resistance associated with the bottom meniscus becomes greater than the top one due to the sharp-edge-pinning mechanism. This is because the corner angle at the bottom (80° with $\alpha = 10°$, defined in figure 1*a*) is smaller than the top one (90°) as a result of the triangular protrusion. Therefore, the bottom meniscus is pinned whereas the top meniscus continues to advance (figure 1*b*-ii,iii). Such a sharp-edge-pinning effect, which is also termed the 'capillary valve effect', has been examined thoroughly in the literature and incorporated into numerical algorithms for simulating multiphase flow in porous media with irregular geometries (Wang, Pereira & Gan 2021; Wang *et al.* 2022).

Once the top meniscus reaches the rear (right) side of the channel, its capillary resistance increases due to the geometrical contraction, resulting in greater capillary resistance compared with the bottom one (since $h_{neck} < h_{top}$). This leads to the movement of the bottom meniscus, triggering the start of the Haines jump: as the bottom meniscus expands into the bottom channel with $h_{bot} = 1$ mm, the smaller capillary resistance within the bottom channel compared with the top one results in the fast retraction of the top meniscus and advancement of the bottom meniscus (figure 1*b*-iv,v). As we will show later, the liquid redistribution process occurs at a much faster speed than the injection velocity, a typical signature of Haines jumps in the capillary-dominated flow regime during the fluid displacement process.

We point out that the expansion angle on the left of the bottom channel α is set to a relatively small value of 10°. This is because a residual defending fluid film can be developed when the geometrical expansion is large (e.g. when $\alpha = 45°$), where the fluid interface becomes unstable and an invading fluid finger grows into the defending fluid, leaving the contact line behind. The critical criterion for the development of the liquid film depends on various factors such as the contact angle and interface velocity, and was examined by Zhao *et al.* (2018), who found that a sudden geometrical expansion during the fluid displacement promotes the development of a liquid film. As a result, a small value of $\alpha = 10°$ is chosen in the current work, such that the unstable interface growth is absent.

2.2. *Numerical scheme*

The numerical simulations for the two-dimensional (2-D) multiphase flow process in the dual-channel system were performed using the laminar two-phase flow-phase-field model implemented in COMSOL Multiphysics 6.1. The governing equations for fluid motion include the continuity and momentum equations

$$\boldsymbol{\nabla} \cdot \boldsymbol{U} = 0, \tag{2.1}$$

$$\rho \left[\frac{\partial \boldsymbol{U}}{\partial t} + (\boldsymbol{U} \cdot \boldsymbol{\nabla})\boldsymbol{U} \right] = \boldsymbol{\nabla} \cdot [\mu(\boldsymbol{\nabla U} + (\boldsymbol{\nabla U})^{\mathrm{T}})] - \boldsymbol{\nabla} P + \boldsymbol{F}_{st}, \tag{2.2}$$

where ρ and μ are the mass density and dynamic viscosity of the fluid, $\boldsymbol{U}$ and P are the flow velocity and pressure while $\boldsymbol{F}_{st}$ is the surface tension force acting at the fluid–fluid interface.

The phase-field method is used for interface tracking and shape modelling, from which the surface tension force $\boldsymbol{F}_{st}$ in the momentum equation can be calculated. The order parameter in phase-field models ϕ describes the distribution of different phases in the system. When $\phi = 1$, the fluid behaves with the property of the invading phase; when $\phi = -1$, the fluid behaves with the property of the defending phase; and $\phi = 0$ corresponds to the fluid–fluid interface location. The effective fluid properties including density ρ and viscosity μ are calculated based on ϕ using linear interpolation between the two fluids.

The governing equation for the phase field is the advective Cahn–Hilliard equation (Cahn & Hilliard 1959)

$$\frac{\partial \phi}{\partial t} + \boldsymbol{U} \cdot \boldsymbol{\nabla} \phi = \boldsymbol{\nabla} \cdot \frac{\lambda f}{\varepsilon^2} \boldsymbol{\nabla} \psi, \tag{2.3}$$

where ε is a capillary width representative of the interface thickness, f is the magnitude of the mixing energy, which satisfies $f = 3\epsilon\sigma/\sqrt{8}$ with σ the surface tension, and λ is the mobility parameter that controls the rate at which concentration differences are 'smoothed out' by diffusion driven by the chemical potential ψ

$$\psi = -\boldsymbol{\nabla} \cdot \varepsilon^2 \boldsymbol{\nabla} \phi + \phi(\phi^2 - 1). \tag{2.4}$$

Subsequently, the surface tension force for the momentum equation is determined by

$$\boldsymbol{F}_{st} = G \boldsymbol{\nabla} \phi, \tag{2.5}$$

$$G = f \left[-\nabla^2 \phi + \frac{\phi(\phi^2 - 1)}{\varepsilon^2} \right] = \frac{f}{\varepsilon^2} \psi. \tag{2.6}$$

We refer the readers to Yue *et al.* (2004) for a detailed description of the phase-field model.

Constant injection velocity and constant pressure boundary conditions are applied at the inlet and outlet, respectively,

$$\boldsymbol{U}_{in} = [V_{in} \quad 0]^{\mathrm{T}}, \tag{2.7}$$

$$P_{out} = 0. \tag{2.8}$$

The no-slip wall condition is adopted at all solid boundaries.

The computational domain was meshed using triangular elements with a total number of elements of 28 995 and a mesh size ranging from 7.2×10^{-4} to 0.05 mm, which are found to be sufficient to give converged results. The maximum element growth rate and curvature factor are set to 1.1 and 0.25, respectively. Simulations were carried out on a Dell workstation (Precision 7920) equipped with an Intel Xeon processor (Gold 6128), and cases in table 1 each take approximately 2 h.

3. Results and discussion

3.1. *Interface motion during Haines jump in the dual-channel system*

To characterise the fluid redistribution process during the Haines jump for the case in figure 1(*b*), the evolution of the bottom channel meniscus velocity u_{bot} is plotted in figure 2(*a*), highlighting four distinct regimes: in regime I the bottom meniscus slowly advances as more invading fluid is injected. In regime II, the bottom meniscus expands into the channel with increasing width (varying from h_{top} to h_{bot} with the inclination angle defined by α), which is associated with decreasing capillary resistance. In regime III, both top and bottom menisci move within the respective channels with uniform widths (h_{top} for the top channel and h_{bot} for the bottom channel). Finally, the Haines jump finishes when the top meniscus reaches the left-most turn, which is accompanied by an oscillation in the top and bottom menisci due to inertia. The bottom meniscus then advances again at a much lower speed (regime IV). The liquid distributions at these regimes are shown in figure 2(*b*). See supplementary movie 1 available at https://doi.org/10.1017/jfm.2024.1225 for the Haines jump phenomenon, and movie 2 for the complete process.

To gain insights into the fluid property-dependent behaviour of the meniscus velocity during the Haines jump, we focus our attention on regime III, during which both top

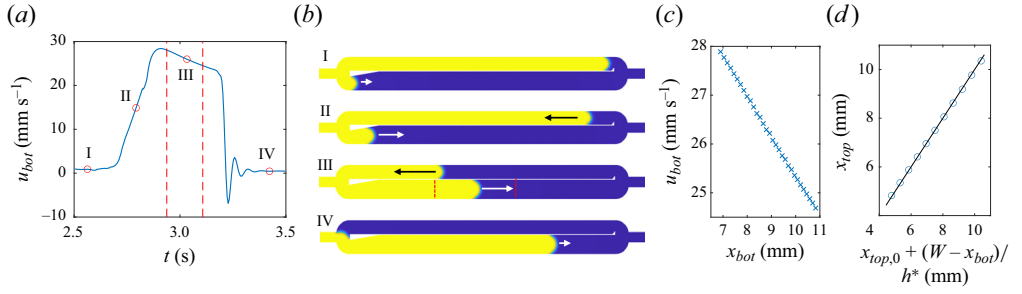

Figure 2. Interface dynamics during a Haines jump (case 4). (*a*) The velocity of the bottom meniscus u_{bot} as a function of time. (*b*) Snapshots of liquid distribution at four stages during the Haines jump. The region between the red-dashed lines in (*a*) and in (*b*-III) indicates the spatial domain where subsequent analysis is based. Arrows indicate meniscus movement direction. (*c*) Value of u_{bot} as a function of location x_{bot}. (*d*) The interface location of the top meniscus x_{top} inferred from x_{bot}.

and bottom menisci move within channels with constant widths. This corresponds to the period in which the location of the bottom meniscus x_{bot} is between the red-dashed lines in figure 2(*a*,*b*). Since u_{bot} is a result of the competition between capillary and viscous forces, and the capillary contrast that drives the motion of fluids remains constant, the decrease in u_{bot} observed in regime III implies that the total viscous dissipation is increasing. Given that the fluid viscosities remain unchanged, the reason for such increased viscous resistance, intuitively, resides in the migration of the more viscous fluid (defending fluid) into the narrower (top) channel, which causes the increase of viscous dissipation for the whole system. We note that the fast fluid redistribution in regime III is effectively a counterclockwise fluid circulation within the channel, as the meniscus travels at a much larger speed ($\sim$25 mm s^{-1}) than the injection velocity of 1 mm s^{-1}. Figure 2(*c*) shows that, as expected, u_{bot} decreases with x_{bot}. Although the focus is placed on tracking the bottom meniscus, the top meniscus location x_{top} can be derived from x_{bot} based on the conservation of mass (inset in figure 2*c*).

3.2. *Analytical model*

The dynamics of the menisci motion during Haines jumps is governed by the balance between the driving capillary force and the dissipating viscous force. The capillary pressure can be described by the Young–Laplace equation $\Delta P = \sigma(1/r_{in} + 1/r_{out})$, where σ, r_{in} and r_{out} represent the interfacial tension, in-plane and out-of-plane curvatures, respectively. Therefore, the capillary pressure contrast between the top and bottom channels is

$$\Delta P_c = \Delta P_{top} - \Delta P_{bot} = \sigma\left(\frac{1}{r_{top,in}} + \frac{1}{r_{top,out}}\right) - \sigma\left(\frac{1}{r_{bot,in}} + \frac{1}{r_{bot,out}}\right). \tag{3.1}$$

For a Hele-Shaw cell system with a uniform depth D, (3.1) becomes

$$\Delta P_c = 2\sigma\left(\frac{\cos\theta_{top}}{h_{top}} + \frac{\cos\theta_{top}}{D}\right) - 2\sigma\left(\frac{\cos\theta_{bot}}{h_{bot}} + \frac{\cos\theta_{bot}}{D}\right). \tag{3.2}$$

The contact angles at the top and bottom channels can be different due to the contact angle hysteresis (Shi *et al.* 2018), i.e. the difference between the contact angles during advancing and receding processes as a result of surface imperfections such as roughness

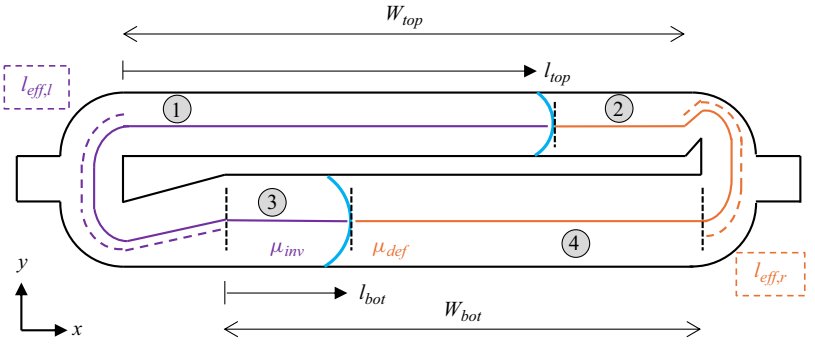

Figure 3. A schematic showing the flow segmentation in the dual-channel geometry (not to scale). Vertical black-dashed lines divide the circulated flow path into four segments.

and chemical heterogeneity. We note that, due to the channel geometry remaining uniform for each meniscus during Haines jumps (stage III in figure 2*b*), the capillary contrast ΔP_c that drives the fluid circulation can be regarded as constant.

For viscous dissipation, figure 3 shows the schematic of flow segmentation during the Haines jump (fast circulation process). The vertical black-dashed lines divide the flow path into four segments. The total viscous pressure drop of the system during the fluid circulation can be calculated via the summation of individual contributions of different flow segments

$$\Delta P_v = \Delta P_{v,1} + \Delta P_{v,2} + \Delta P_{v,3} + \Delta P_{v,4}. \tag{3.3}$$

For laminar Newtonian flow, one should expect a linear relationship between the flow rate and pressure drop

$$\Delta P_v = \frac{\mu_{inv} L_1}{k_1} u_{top} + \frac{\mu_{def} L_2}{k_2} u_{top} + \frac{\mu_{inv} L_3}{k_3} u_{bot} + \frac{\mu_{def} L_4}{k_4} u_{bot}, \tag{3.4}$$

where L is the effective segment length. Here, k is the permeability of the corresponding segment. Despite commonly being used in porous medium flow, here, the term 'permeability' is adopted for channel flows as it captures the geometrical feature while being independent of the fluid property, as opposed to 'hydraulic conductivity'. The permeability of Newtonian flow in a rectangular channel of width h and depth D is (Boussinesq 1868; White 1991)

$$k = \frac{h^2}{12}\left[1 - \frac{192h}{\pi^5 D}\sum_{n=1}^{\infty}\frac{1}{(2n-1)^2}\tanh\frac{(2n-1)\pi D}{2h}\right]. \tag{3.5}$$

When the channel depth D is much greater than the width h, (3.5) is approximated by $k = h^2/12$. (Note that the viscous pressure drop for non-Newtonian flow is more complex due to the shear-rate-dependent viscosity. We refer readers to Chun *et al.* (2024) and Boyko & Stone (2021) for recent studies on the pressure drop of a Carreau fluid in rectangular channels.)

For the considered geometry and flow pathway segmentation shown in figure 3, the channel lengths of each segment are $L_1 = l_{top} + l_{eff,l}$, $L_2 = W_{top} - l_{top} + l_{eff,r}$, $L_3 = l_{bot}$ and $L_4 = W_{bot} - l_{bot}$, where $l_{eff,l}$ and $l_{eff,r}$ are the effective channel lengths on the left (purple-dashed line) and right side (orange-dashed line), respectively. Additionally, with uniform channel depth D, $k_1 = k_2 = k_{top}$ (same channel width h_{top}) and $k_3 = k_4 = k_{bot}$

(same channel width h_{top}). We define the channel width contrast $h^* = h_{top}/h_{bot}$. The meniscus location in the top channel l_{top} can be expressed as a function of the bottom meniscus location l_{bot} using conservation of mass via $l_{top} = l_{top,0} + (W_{bot} - l_{bot})/h^*$, with $l_{top,0}$ being a reference location (figure 2*c*). Similarly, the meniscus velocity in the top channel can be expressed as a function of the bottom meniscus velocity and the channel width contrast: $u_{top} = u_{bot}/h^*$. Here, we have assumed that the inlet velocity u_{in} is much smaller than the meniscus velocities during the Haines jumps, i.e. the invading fluid volume injected during the Haines jump is ignored. The error associated with this assumption will be discussed later. With the expressions above and by balancing $\Delta P_c = \Delta P_v$, (3.4) can be rearranged into the following form:

$$u_{bot} = \frac{\Delta P_c}{p l_{bot} + q}, \tag{3.6}$$

where

$$p = \frac{\mu_{def} - \mu_{inv}}{k_{bot}} \left(\frac{1}{h^{*2}} \frac{k_{bot}}{k_{top}} - 1 \right), \tag{3.7}$$

$$q = \mu_{inv} \frac{l_{top,0} + l_{eff,l} + W_{bot}/h^*}{h^* k_{top}} + \mu_{def} \left(\frac{W_{top} + l_{eff,r} - l_{top,0} - W_{bot}/h^*}{h^* k_{top}} + \frac{W_{bot}}{k_{bot}} \right). \tag{3.8}$$

Since in the considered channel geometry $h_{bot} > h_{top}$, $h^* = h_{top}/h_{bot} < 1$ and $k_{bot} > k_{top}$, the term within the bracket in (3.7) is positive, which reveals three distinct regimes for the behaviour of the bottom meniscus movement velocity u_{bot} as the Haines jump proceeds (increasing l_{bot}). When the defending fluid is more viscous, $p > 0$ and u_{bot} decreases with increasing l_{bot}; whereas u_{bot} will increase with l_{bot} when the invading fluid is more viscous. When both fluids have the same viscosity, $p = 0$, and the meniscus velocity remains constant.

In the following, we first examine the proposed model with 2-D numerical simulations ($D \gg h$) with varied fluid properties. Then, results when the channel depth is comparable to the width are discussed.

3.3. *Numerical simulation*

Our 2-D numerical simulation of Newtonian fluids corresponds to the cases where the channel depth is much greater than the channel width, and the channel width dominates the viscous dissipation. The fluid properties, including the viscosities of invading and defending fluids, interfacial tension and contact angle are varied, and are summarised in table 1. A constant inlet velocity $V_{in} = 1$ mm s^{-1} is imposed for all simulations.

Figure 4(*a*) plots the velocity of the bottom meniscus u_{bot} as a function of its location l_{bot} during Haines jumps. It can be seen that u_{bot} can either increase, decrease or remain constant depending on the relative magnitude of μ_{inv} to μ_{def}, consistent with the theory.

By defining the viscosity ratio $M = \mu_{def}/\mu_{inv}$, and using $k = h^2/12$ for the permeability, one obtains the governing equation that captures the competition between

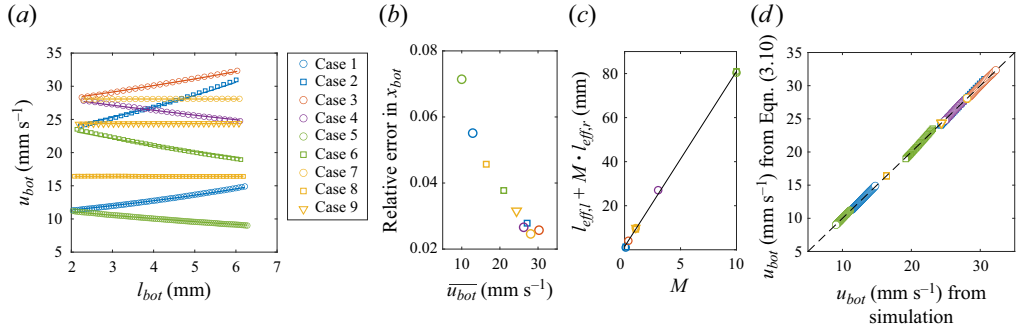

Figure 4. Model validation of the interface dynamics during a Haines jump. (*a*) Bottom interface velocity u_{bot} as a function of location l_{bot}. Refer to table 1 for fluid properties. (*b*) The relative error in the bottom meniscus location estimation as a function of average bottom meniscus velocity during Haines jumps. (*c*) A linear relation between the viscosity ratio M and the term $l_{eff,l} + Ml_{eff,r}$ demonstrates the fluid property independence of the fitting parameters $l_{eff,l}$ and $l_{eff,r}$. (*d*) Comparison between u_{bot} from simulation and calculated from (3.9). Note that the overlaps of yellow markers are due to the constant velocity under $M = 1$ (horizontal lines in (*a*)).

viscous and capillary forces during the Haines jump in the dual-channel system

$$(1-M)\left(l_{top,0} + \frac{W_{bot}}{h^*}\right) + M(W_{top} + h^{*3}W_{bot}) + l_{eff,l} + Ml_{eff,r} + (h^{*3}-1)(1-M)l_{bot} = \frac{\sigma(\cos\theta_{top} - h^*\cos\theta_{bot})h^*h_{top}}{6\mu_{inv}} \cdot \frac{1}{u_{bot}}. \tag{3.9}$$

The only parameters in (3.9) that need fitting are the geometry-dependent $l_{eff,l}$ and $l_{eff,r}$, which represent the effective channel lengths due to the curved channels at the left and right sides, indicated by the purple and orange dashed curves in figure 3, respectively. Figure 4(*c*) shows the term $l_{eff,l} + M \cdot l_{eff,r}$ as a function of the viscosity ratio M for all nine cases listed in table 1, and the fitted values are $l_{eff,l} = 1.4$ mm and $l_{eff,r} = 7.9$ mm, where fitting was done using the default least-squares algorithm available in the *fit* function in *MATLAB*. The strong linear trend with a coefficient of determination $R^2 = 0.999$ evidences that $l_{eff,l}$ and $l_{eff,r}$ are indeed fluid-property-independent. This means that, once these parameters are fitted (model calibration process), (3.9) can be used to describe processes with different fluid properties without the need for further fitting.

To quantify the error induced by ignoring the inlet velocity in the model, figure 4(*b*) plots the relative error in estimating the top meniscus location using the bottom one based on mass conservation without taking into account the additional invading fluid injected from the inlet during Haines jumps. The relative error is calculated by the absolute error in meniscus location divided by the total distance travelled during Haines jumps. As expected, the error decreases with the average bottom meniscus velocity during Haines jumps. The maximum error occurs when the meniscus velocity is minimum (case 5), leading to an error of around 0.3 mm. However, this error is still less than 10 % of the distance travelled by the bottom meniscus during Haines jumps (a relative error of less than 0.1 in figure 4*b*).

To validate (3.9), figure 4(*d*) compares the value of u_{bot} obtained from numerical simulation and u_{bot} calculated from (3.9), showing a good agreement. The markers in yellow appear to be a single point on figure 4(*d*). This is because the overlaps of u_{bot} that remain constant during Haines jumps due to the viscosity ratio $M = 1$.

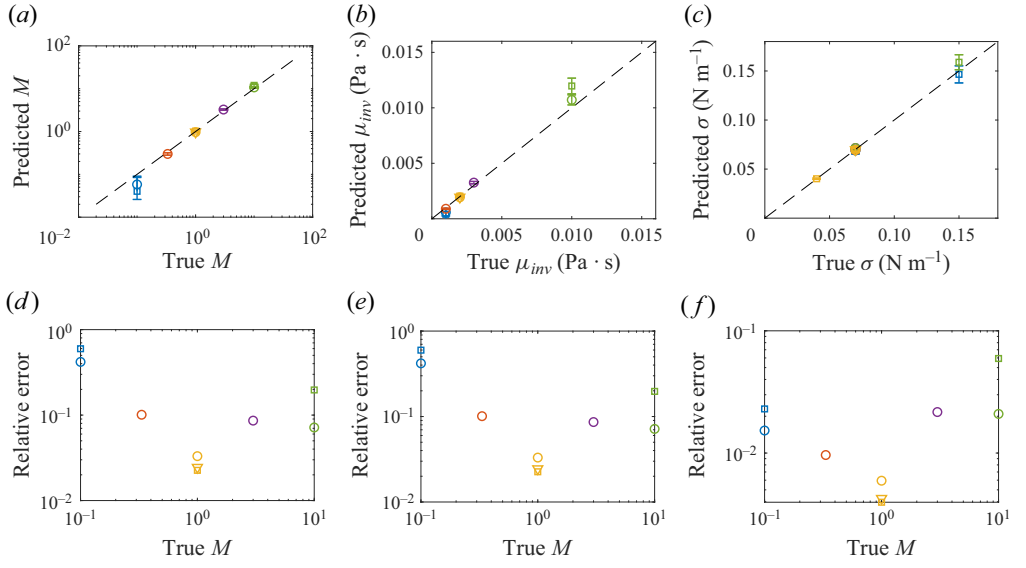

Figure 5. Simultaneous determination of fluid properties during a Haines jump. (*a*) Viscosity ratio M, (*b*) viscosity of the invading fluid μ_{inv} and (*c*) interfacial tension. Refer to the legend in figure 4(*a*) for marker meaning. (*d–f*) The corresponding relative errors of the predicted values on the top panels as a function of the viscosity ratio.

3.4. *Simultaneous determination of viscosity and interfacial tension*

By examining (3.9), we notice that, apart from the fluid property-related terms M and σ/μ_{inv}, all other parameters can be determined from the geometry (W_{bot}, W_{top}, h_{bot}, h_{top}, $l_{eff,l}$, $l_{eff,r}$) or measured during the Haines jump process (l_{bot}, u_{bot}, $\cos\theta_{bot}$, $\cos\theta_{top}$). As a result, the values of M and σ/μ_{inv} can be determined by analysing the dynamics of meniscus movement during Haines jumps. In the case where, for example, the defending fluid viscosity μ_{def} is known, the interfacial tension σ and viscosity of the invading fluid μ_{inv} can be simultaneously calculated using (3.9) based on the measured bottom meniscus location, velocity and contact angles at the bottom and top channel during the Haines jumps.

Figure 5 shows the comparisons between predicted values of fluid properties and the respective true values (marker legend meaning is the same as figure 4*a*). The error bars represent one standard deviation considering the uncertainties from: (i) measurement uncertainty from simulation results, including the fluctuations in the measured advancing and receding contact angles and uncertainty in interface location (i.e. the difference between the locations of the interface tip along the channel centre and the triple-contact lines); (ii) fitting uncertainty in the fitted values of $l_{eff,l}$ and $l_{eff,r}$ with confidence interval 0.68; and (iii) model error, which is induced from the assumption that the inlet velocity can be ignored during the Haines jump (as discussed in the previous section and figure 4*b*). Further, the corresponding relative errors in figure 5(*a–c*), calculated as |true-predicted|/true, are plotted in figure 5(*d–f*). We see that the relative errors become greater as the viscosity ratio M deviates from unity, leading to a relative error in the predicted μ_{inv} as large as 0.59 for $M = 0.1$. This reveals that the intrinsic errors (aforementioned measurement uncertainty, fitting uncertainty and model assumption) are magnified as the fluid viscosity contrast is greater. Nevertheless, the relative errors in the surface tension prediction remain less than 10 % in the range $M \in [0.1, 10]$. Note that

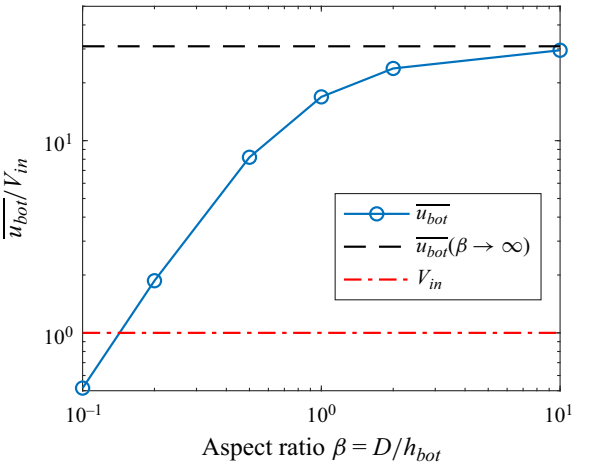

Figure 6. The average bottom meniscus movement velocity $\overline{u_{bot}}$ during Haines jumps normalised by the inlet velocity V_{in} under different β. The black-dashed line represents the 2-D scenario.

the results in figure 5(*d*,*e*) are identical, since figure 5(*a*,*b*) essentially contains the same information scaled by μ_{def}.

3.5. *Effect of channel depth*

In previous sections, we have focused on 2-D cases corresponding to a channel geometry with a depth D much greater than the width h, such that the calculation of permeability is simplified to $k = h^2/12$ according to (3.5). Practically, such microfluidic devices can be manufactured using the selective laser etching technique (Gottmann, Hermans & Ortmann 2012), an example of which is the porous medium micromodel with a depth-to-post diameter ratio of 20 (Haward, Hopkins & Shen 2021). However, in other conventional methods for microfluidic device fabrication, such as soft lithography, the aspect ratio may not be so large and the effect of channel depth cannot be ignored. In such cases, the permeability is calculated using (3.5). As (3.5) quickly converges as the number of terms N increases, $N = 5$ is used for the calculation of permeability, where a less than 0.1 % variation is observed as N further increases.

To quantitatively explore the effect of channel depth on the flow in the dual-channel system, we define the aspect ratio $\beta = D/h_{bot}$. The average bottom meniscus velocity $\overline{u_{bot}}$ normalised by the injection velocity V_{in} is plotted as a function of β in figure 6. The fluid properties of case 7 are used for calculation. The black-dashed line and red-dot-dashed line, respectively, represent the meniscus velocity for the 2-D case ($\beta \to \infty$) and the injection velocity $V_{in} = 1$ mm s^{-1} in the simulation. The meniscus velocity decreases from its maximum as β decreases, reaching below the currently imposed V_{in} at $\beta = 0.1$. This means that a much smaller injection velocity is required to ensure that the speed of interface motion during Haines jumps is much greater than V_{in}. In rectangular channels, aspect ratios β of 10, 1 and 0.1 lead to the actual permeability (and meniscus velocity) being 94 %, 42 % and 1 % of the value for a 2-D scenario ($\beta \to \infty$). This highlights that a large aspect ratio is desired whereas a small aspect ratio can lead to a drastic reduction of meniscus velocity.

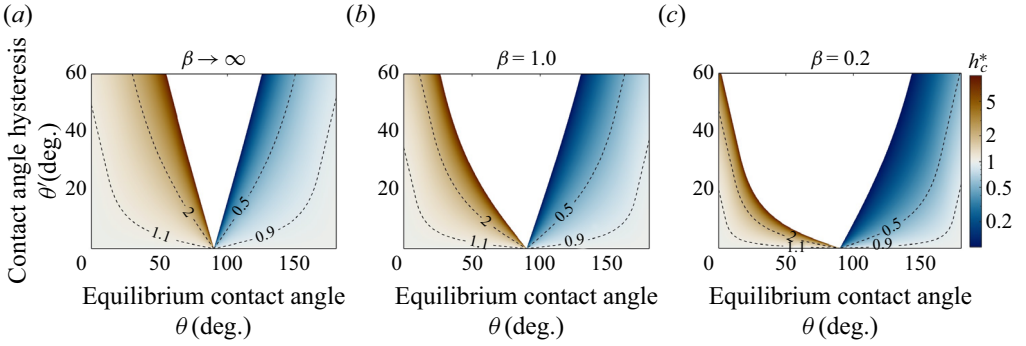

Figure 7. Effect of contact angle hysteresis. Contour map showing the critical width contrast h_c^* required for Haines jumps as a function of equilibrium contact angle and contact angle hysteresis for (*a*) $\beta \to \infty$ (corresponding to the 2-D case), (*b*) $\beta = 1$ and (*c*) $\beta = 0.2$.

3.6. *Discussion*

In the design of the dual-channel system as well as the numerical simulations, we have considered drainage processes for which the contact angle is greater than 90°. However, we emphasise that the same analysis, namely the competition between viscous and capillary forces, can also be applied to imbibition processes ($\theta < 90°$). Similarly, it is possible to design dual-channel geometries with different channel widths and the placement of barriers to create hierarchies of capillary pressures. Although Haines jumps are commonly referred to in drainage processes, the same physical phenomenon, i.e. rapid fluid interface motion accompanied by liquid redistribution and pressure fluctuations, are also present in imbibition processes (Zhao, MacMinn & Juanes 2016; Primkulov *et al.* 2022).

An important requirement for the applicability of the current approach is the existence of the actuation force that originates from the differences in capillary pressure between the top and bottom menisci (described in (3.1)). However, the contact angle hysteresis $\theta' = \theta_{adv} - \theta_{rec}$, i.e. the difference between the advancing (bottom side) and receding (top side) contact angles, can lead to deviations of effective contact angles from the equilibrium ones, which hinders the driving capillary force. In the current work, the contact angle hysteresis in the simulation is small, i.e. the difference between θ_{top} and θ_{bot} (or the difference between θ_{rec} and θ_{adv}) is less than 3°. In practical applications, the contact angle hysteresis can be greater due to surface chemical heterogeneity or roughness. Reducing contact angle hysteresis on engineered surfaces has been an active area of research. For example, Esmaeilzadeh *et al.* (2016) showed that the contact angle hysteresis can be reduced to less than 5° by surface coating of nanoparticles.

To ensure a positive capillary driving force with consideration of contact angle hysteresis, the critical channel width contrast h_{crit}^* should satisfy

$$h_{crit}^* = \frac{\cos\theta_{top}}{\cos\theta_{bot} + 1/\beta(\cos\theta_{bot} - \cos\theta_{top})}, \tag{3.10}$$

where $\cos\theta_{top} = \theta - \theta'/2$, $\cos\theta_{bot} = \theta + \theta'/2$ and $\beta = D/h_{bot}$ represents the aspect ratio of the channel. The contour maps for h_{crit}^* under different β are plotted in figure 7. Here, we consider a practical range of $h_{crit}^* \in [0.1, 10]$. The white region in figure 7 represents the region where the Haines jump cannot take place. It can be seen that the minimum channel contrast is more demanding as: (i) contact angle hysteresis increases; (ii) when the equilibrium contact angle θ approaches the neutral condition ($\theta = 90°$); or (iii) the aspect ratio β decreases, which is associated with the increasing effect of contact angle

hysteresis from the out-of-plane direction. Thus, ensuring homogeneous solid surfaces for small contact angle hysteresis, as well as a non-neutral solid wettability, are critical when manufacturing the physical device. Note that the asymmetry in the contour maps for finite values of β is due to the definition of the aspect ratio being based on the bottom channel width.

Overall, our results (figure 5) highlight that the dual-channel configuration combined with the developed model in the work can provide an effective approach to simultaneously measuring the interfacial tension and fluid viscosity in a multiphase system. Despite acknowledging the existing advanced techniques for fluid property testing, such as those that require force sensing equipment during droplet merger (Nguyen *et al.* 2021), laser-light scattering apparatus (Nishio & Nagasaka 1995) or oscillations of acoustically levitated droplets (Kremer, Kilzer & Petermann 2018) combined with rainbow refractometry (Wu *et al.* 2021) or under a microgravity environment (Fujii *et al.* 2005), we want to highlight the key advantages of the present approach. Firstly, such a method only requires the imaging of the fluid distribution and control of the injection velocity, which is straightforward compared with existing techniques and does not require advanced equipment. Further, the fluid properties are determined by analysing the Haines jump phenomena that occur ubiquitously in fluid–fluid displacement processes in a confined geometry. This means that it is possible to extend the theory for *in situ* fluid property characterisation during multiphase flow in an artificial porous medium that has regular pore structures, where the capillary driving force and viscous dissipation can be accurately quantified. Such non-intrusive real-time characterisation of the fluid property could be particularly important in processes where fluid flow is accompanied by chemical reaction/mass transport (Dudukovic *et al.* 2021; Wang *et al.* 2024).

4. Conclusions

Inspired by the Haines jump mechanisms commonly observed during immiscible fluid displacement processes in porous media, we have designed a dual-channel system with hierarchies of capillary barriers to realise the spontaneous rapid liquid redistribution during multiphase flow. Three regimes of the interface motion behaviours are identified, where the meniscus movement velocity can increase, decrease or remain the same during Haines jumps, depending on the viscosity ratio of the invading and defending fluids. Based on the competition between capillary and viscous forces, an analytical model is developed to describe the dynamics of interface movement during Haines jumps. Results from numerical simulations under different viscosities, surface tensions and contact angles show that the proposed analytical model can well describe the interfacial movement. Further, our analysis demonstrates that the dual-channel system combined with the developed model is capable of simultaneously determining the interfacial tension and fluid viscosity. This work provides fundamental insights into multiphase flow processes, and the results should facilitate the development of alternative approaches for the effective measurement of important fluid properties.

Supplementary movies. Supplementary movies are available at https://doi.org/10.1017/jfm.2024.1225.

Acknowledgements. The authors thank the anonymous reviewers for their constructive feedback.

Funding. This work was supported by the Queensland University of Technology (QUT) MMPE Early Career Researcher (ECR) grant awarded to Z.W., and the Australian Research Council Future Fellowship FT200100446 awarded to E.S.

Declaration of interests. The authors declare no competing interests.

Author ORCIDs.
Zhongzheng Wang https://orcid.org/0000-0001-9456-4744;
Yixiang Gan https://orcid.org/0000-0002-9621-0277;
Jean-Michel Pereira https://orcid.org/0000-0002-0290-5191;
Scott W. McCue https://orcid.org/0000-0001-5304-2384;
Emilie Sauret https://orcid.org/0000-0002-8322-3319.

References

Armstrong, R.T., Evseev, N., Koroteev, D. & Berg, S. 2015 Modeling the velocity field during haines jumps in porous media. *Adv. Water Resour.* **77**, 57–68.

Berg, S., *et al*. 2013 Real-time 3D imaging of haines jumps in porous media flow. *Proc. Natl Acad. Sci.* **110** (10), 3755–3759.

Boussinesq, J. 1868 Mémoire sur l'influence des Frottements dans les Mouvements Réguliers des Fluids. *J. Math. Pures Appl.* **13** (2), 377–424.

Boyko, E. & Stone, H.A. 2021 Flow rate–pressure drop relation for shear-thinning fluids in narrow channels: approximate solutions and comparison with experiments. *J. Fluid Mech.* **923**, R5.

Cahn, J.W. & Hilliard, J.E. 1959 Free energy of a nonuniform system. III. Nucleation in a two-component incompressible fluid. *J. Chem. Phys.* **31** (3), 688–699.

Chun, S.G., Boyko, E., Christov, I.C. & Feng, J. 2024 Flow rate–pressure drop relations for shear-thinning fluids in deformable configurations: theory and experiments. *Phys. Rev. Fluids* **9**, 043302.

Dudukovic, N.A., Fong, E.J., Gemeda, H.B., DeOtte, J.R., Cerón, M.R., Moran, B.D., Davis, J.T., Baker, S.E. & Duoss, E.B. 2021 Cellular fluidics. *Nature* **595** (7865), 58–65.

Esmaeilzadeh, P., Sadeghi, M.T., Bahramian, A., Fakhroueian, Z. & Zarbakhsh, A. 2016 Superamphiphobic surfaces prepared by coating multifunctional nanofluids. *ACS Appl. Mater. Interfaces* **8** (46), 32011–32020.

Fujii, H., Matsumoto, T., Ueda, T. & Nogi, K. 2005 A new method for simultaneous measurement of surface tension and viscosity. *J. Mater. Sci.* **40** (9), 2161–2166.

Furuberg, L., Måløy, K.J. & Feder, J. 1996 Intermittent behavior in slow drainage. *Phys. Rev.* E **53**, 966–977.

Gottmann, J., Hermans, M. & Ortmann, J. 2012 Digital photonic production of micro structures in glass by in-volume selective laser-induced etching using a high speed micro scanner. *Phys. Procedia* **39**, 534–541.

Haines, W.B. 1930 Studies in the physical properties of soil. V. The hysteresis effect in capillary properties, and the modes of moisture distribution associated therewith. *J. Agric. Sci.* **20** (1), 97–116.

Haward, S.J., Hopkins, C.C. & Shen, A.Q. 2021 Stagnation points control chaotic fluctuations in viscoelastic porous media flow. *Proc. Natl Acad. Sci.* **118** (38), e2111651118.

Heinemann, N., *et al*. 2021 Enabling large-scale hydrogen storage in porous media – the scientific challenges. *Energy Environ. Sci.* **14**, 853–864.

Holtzman, R., Dentz, M., Planet, R. & Ortín, J. 2023 The relation between dissipation and memory in two-fluid displacements in disordered media. *Geophys. Res. Lett.* **50** (16), e2023GL104073.

Jang, J., Sun, Z. & Santamarina, J.C. 2016 Capillary pressure across a pore throat in the presence of surfactants. *Water Resour. Res.* **52** (12), 9586–9599.

Kremer, J., Kilzer, A. & Petermann, M. 2018 Simultaneous measurement of surface tension and viscosity using freely decaying oscillations of acoustically levitated droplets. *Rev. Sci. Instrum.* **89** (1), 015109.

Lake, L.W., Johns, R., Rossen, B. & Pope, G. 2014 *Fundamentals of Enhanced Oil Recovery*. Society of Petroleum Engineers.

Moebius, F. & Or, D. 2012 Interfacial jumps and pressure bursts during fluid displacement in interacting irregular capillaries. *J. Colloid Interface Sci.* **377** (1), 406–415.

Nguyen, T.-V., Okada, H., Okamoto, Y., Takei, Y., Takei, A. & Ichiki, M. 2021 Simultaneous measurement of surface tension and viscosity utilizing droplet merging. In *2021 IEEE 34th International Conference on Micro Electro Mechanical Systems (MEMS)*, pp. 760–763. IEEE.

Nishio, T. & Nagasaka, Y. 1995 Simultaneous measurement of surface tension and kinematic viscosity using thermal fluctuations. *Intl J. Thermophys.* **16** (5), 1087–1097.

Primkulov, B.K., Zhao, B., MacMinn, C.W. & Juanes, R. 2022 Avalanches in strong imbibition. *Commun. Phys.* **5** (1), 52.

SHI, Z., ZHANG, Y., LIU, M., HANAOR, D.A.H. & GAN, Y. 2018 Dynamic contact angle hysteresis in liquid bridges. *Colloids Surf. A: Physicochem. Engng Aspects* **555**, 365–371.

SUN, Z. & SANTAMARINA, J.C. 2019 Haines jumps: pore scale mechanisms. *Phys. Rev.* E **100**, 023115.

SZULCZEWSKI, M.L., MACMINN, C.W., HERZOG, H.J. & JUANES, R. 2012 Lifetime of carbon capture and storage as a climate-change mitigation technology. *Proc. Natl Acad. Sci.* **109** (14), 5185–5189.

WANG, Z., ONG, L.J.Y., GAN, Y., PEREIRA, J.-M., ZHANG, J., KASETSIRIKUL, S., TOH, Y.-C. & SAURET, E. 2024 Porofluidics: deterministic fluid control in porous microfluidics. *Lab on a Chip* **24**, 4050–4059.

WANG, Z., PEREIRA, J.-M. & GAN, Y. 2021 Effect of grain shape on quasi-static fluid-fluid displacement in porous media. *Water Resour. Res.* **57** (4), e2020WR029415.

WANG, Z., PEREIRA, J.-M., SAURET, E., ARYANA, S.A., SHI, Z. & GAN, Y. 2022 A pore-resolved interface tracking algorithm for simulating multiphase flow in arbitrarily structured porous media. *Adv. Water Resour.* **162**, 104152.

WHITE, F.M. (Frank Mangrem) 1991 *Viscous Fluid Flow: Frank M. White*, 2nd edn. McGraw-Hill Medical.

WU, Y., LV, Q., WU, X., WANG, X., CHEN, L. & CEN, K. 2021 Simultaneous measurement of surface tension and viscosity of oscillating droplet using time-resolved rainbow refractometry. *Powder Technol.* **391**, 425–431.

YUE, P., FENG, J.J., LIU, C. & SHEN, J. 2004 A diffuse-interface method for simulating two-phase flows of complex fluids. *J. Fluid Mech.* **515**, 293–317.

ZHAO, B., ALIZADEH PAHLAVAN, A., CUETO-FELGUEROSO, L. & JUANES, R. 2018 Forced wetting transition and bubble pinch-off in a capillary tube. *Phys. Rev. Lett.* **120**, 084501.

ZHAO, B., MACMINN, C.W. & JUANES, R. 2016 Wettability control on multiphase flow in patterned microfluidics. *Proc. Natl Acad. Sci.* **113** (37), 10251–10256.